ADVANCED ENERGY MATERIALS

Supporting Information

for *Adv. Energy Mater.*, DOI: 10.1002/aenm.202002637

3D Architected Carbon Electrodes for Energy Storage

Kai Narita, Michael A. Citrin, Heng Yang, Xiaoxing Xia, and Julia R. Greer*

Supporting Information

Title: 3D Architected Carbon Electrodes for Energy Storage

Authors: Kai Narita, Michael A. Citrin, Heng Yang, Xiaoxing Xia, Julia R. Greer*

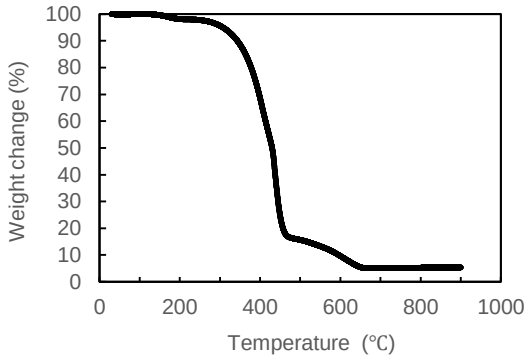

Figure S1 Thermogravimetric analysis (TGA) of acryl-based photoresin under a N_2 flow

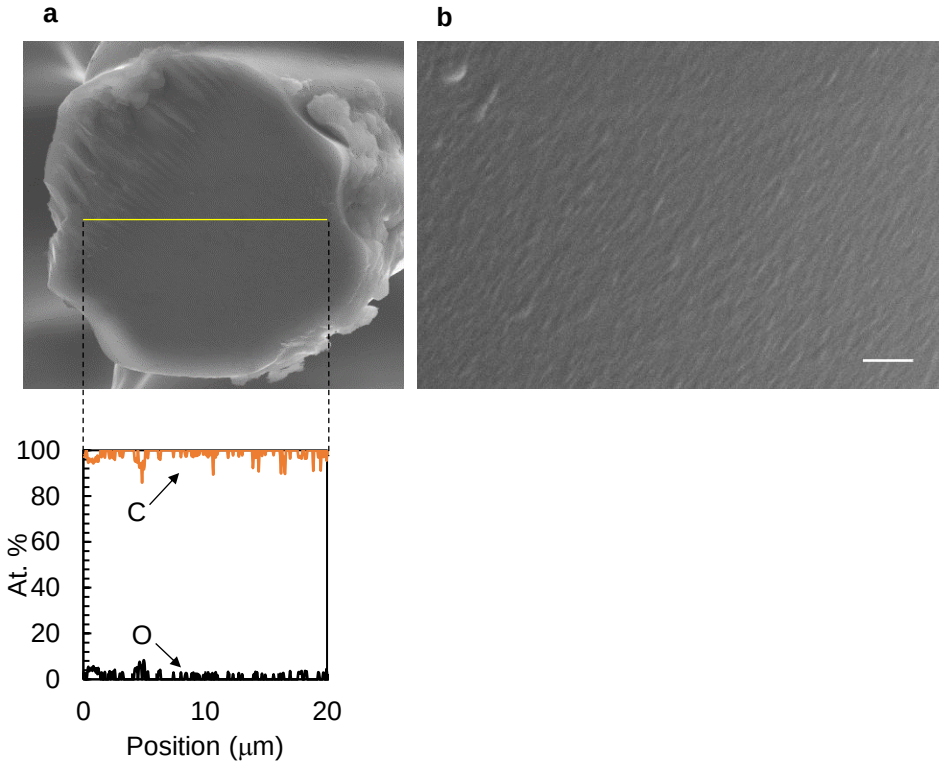

Figure S2 **a** Line analysis of EDS on the cross-section. **b** high resolution SEM image of the 3D architected carbon showing smooth surface. The scale bar in b is 100 nm.

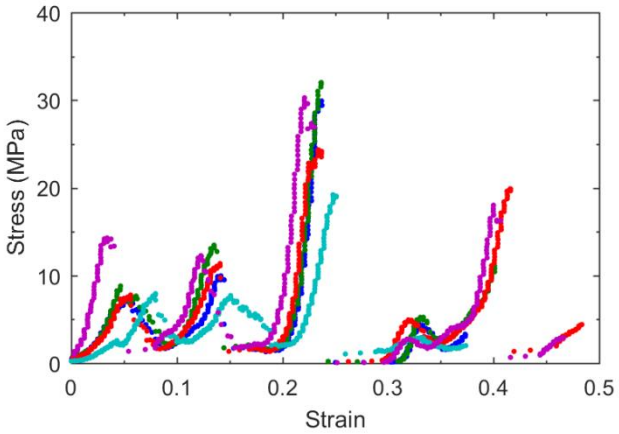

Figure S3 Stress-strain curve of five samples of the 3D architected carbon.

Table S1 Average values and standard deviations of the 1st, 2nd and 3rd yield strength.

	1st yield	2nd yield	3rd yield
Average (MPa)	9.2	14.2	27.1
SD (MPa)	2.9	6.4	5.3

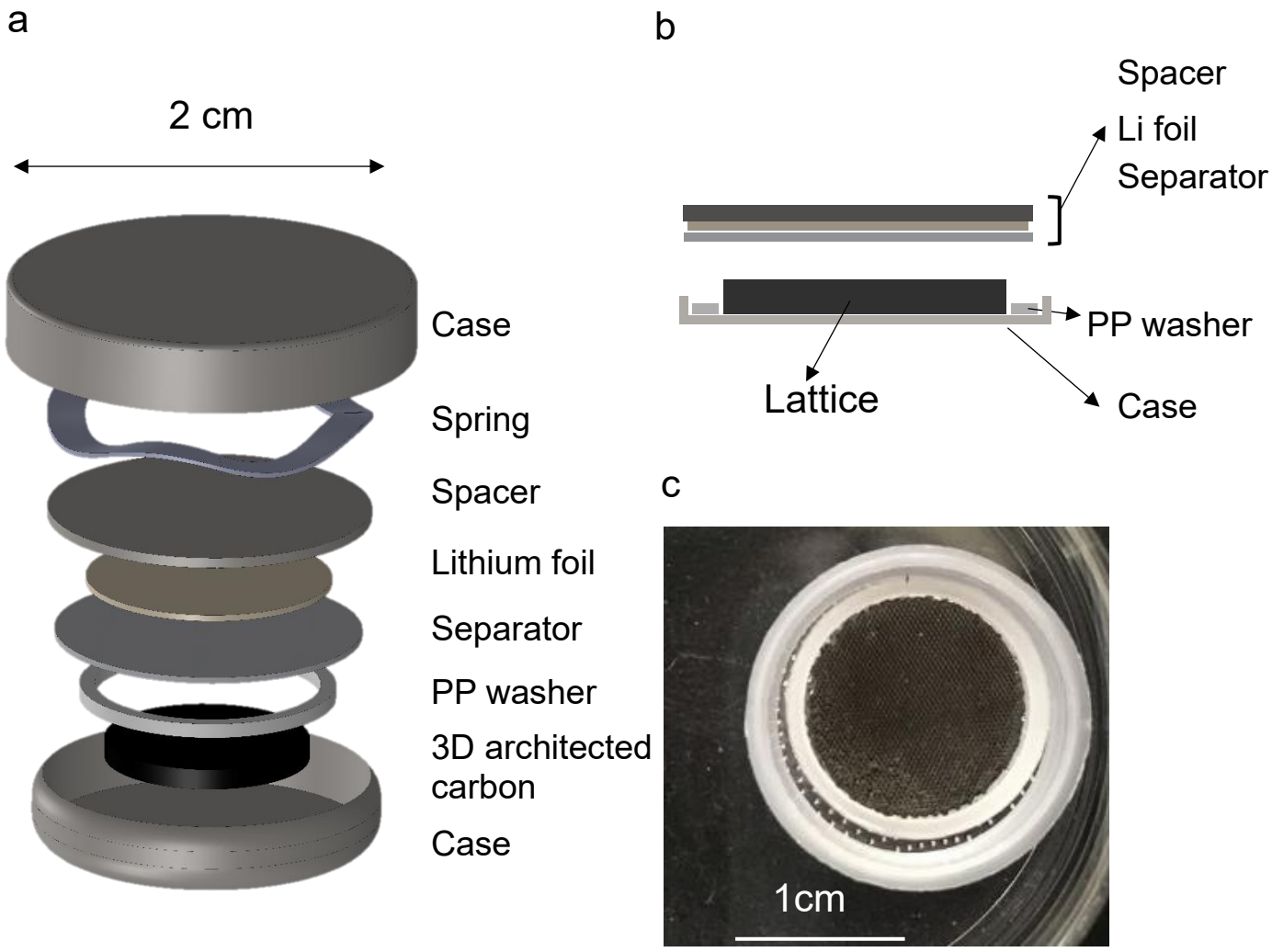

Figure S4 **a** Schematic images of coin cell components. **b** schematic side view of coin cell components (without top case and spring). **c** top view of the 3D architected carbon surrounded by a PP washer on a bottom case

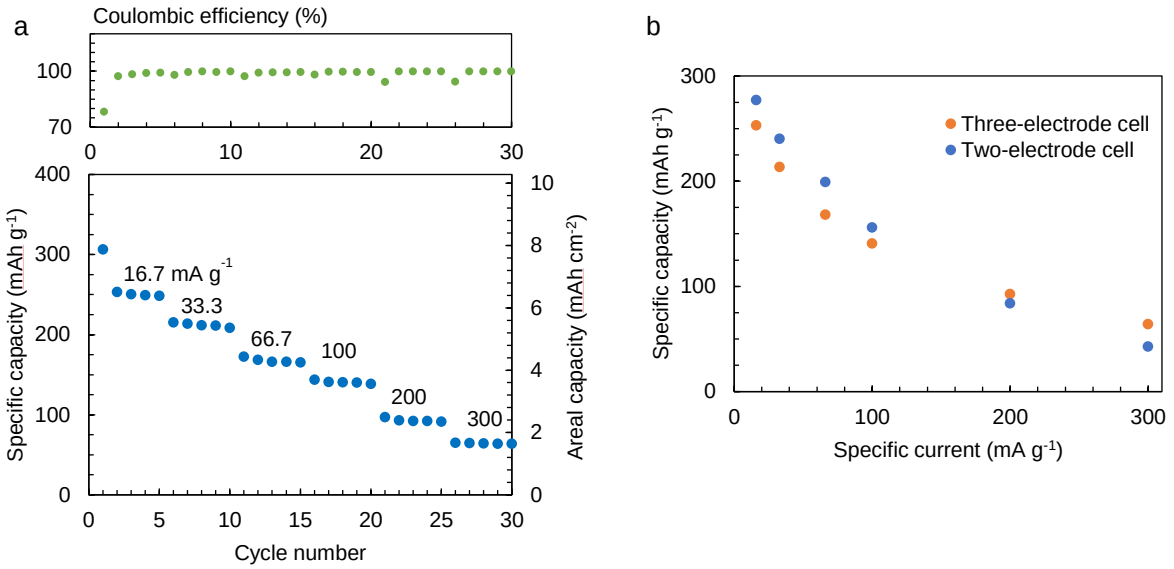

Figure S5 **a** Galvanostatic cycling of architected carbon electrodes using a three-electrode configuration cell. Columbic efficiency (top) and discharge capacities (bottom) at step currents indicated by the number above each segment. **b** Discharge capacities at 2nd cycle in each step current of the architected carbon electrodes cycled in a three-electrode configuration cell shown in **a** and cycled in a two-electrode configuration cell shown in Figure 4b

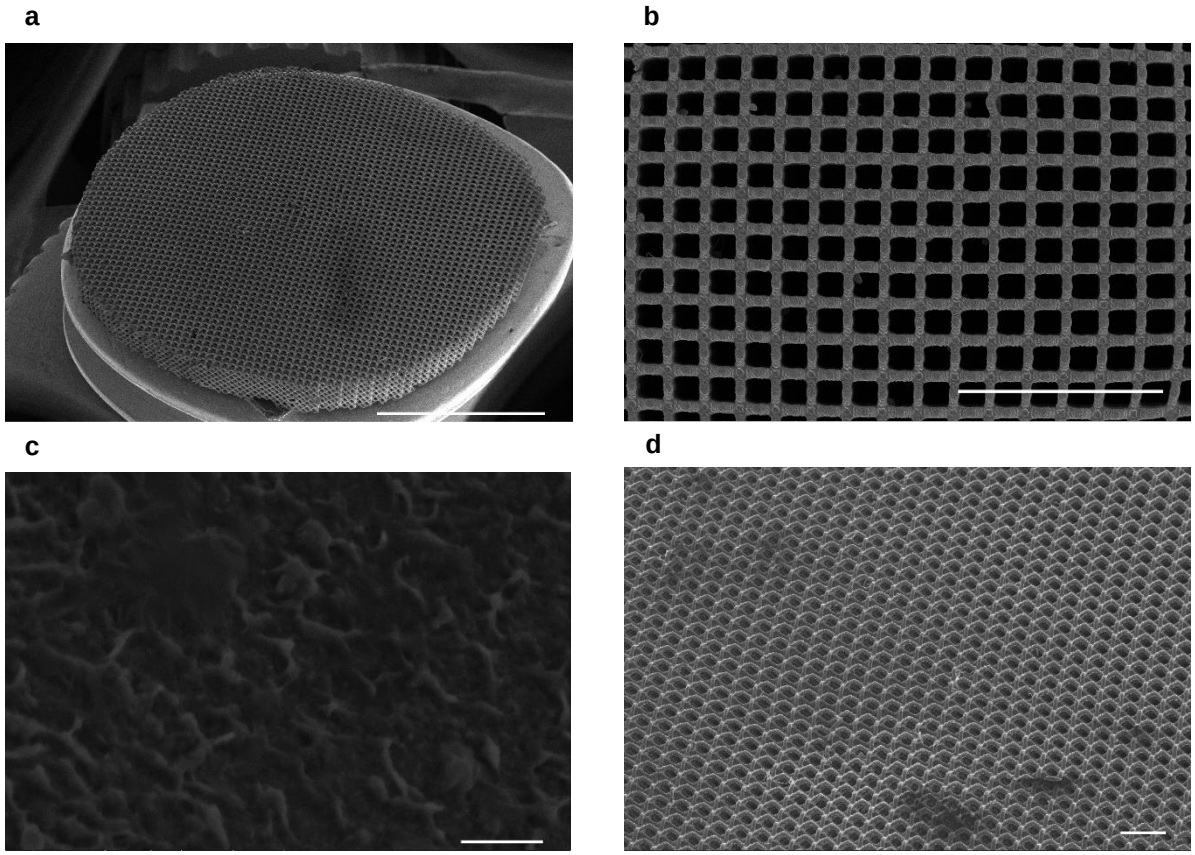

Figure S6 Representative SEM images of the 3D carbon electrodes after >300 cycles at 100 mA g^{-1} in a coin cell **a** whole view, b defected beam pointed by the red circle **c** surface morphology of the beam. **d** SEM image of an 3D carbon electrode after +500 cycles. The scale bars are 5 mm in **a**, 1 mm in b, 500 nm in c, and 400 μm in **d**.

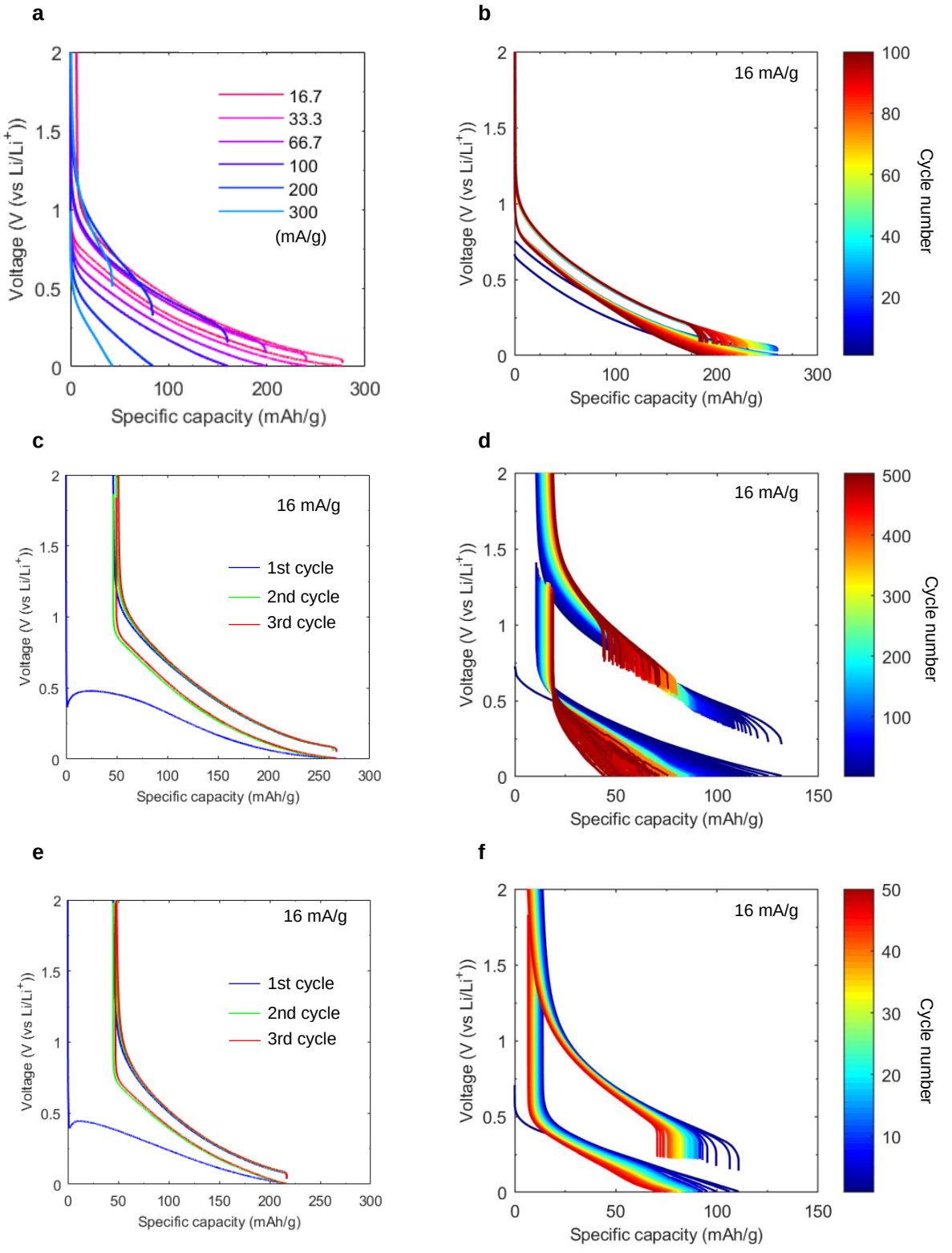

Figure S7 Discharge-charge curves for Figure 3b: **a** at step currents and **b** at 16 mA g^{-1} after step currents. Discharge-charge curves for Figure 3c: **c** at 17 mA g^{-1} as three pre-cycles and **d** at 100 mA g^{-1}, and after recycling **e** at 17 mA g^{-1} as three pre-cycles and **f** at 100 mA g^{-1}

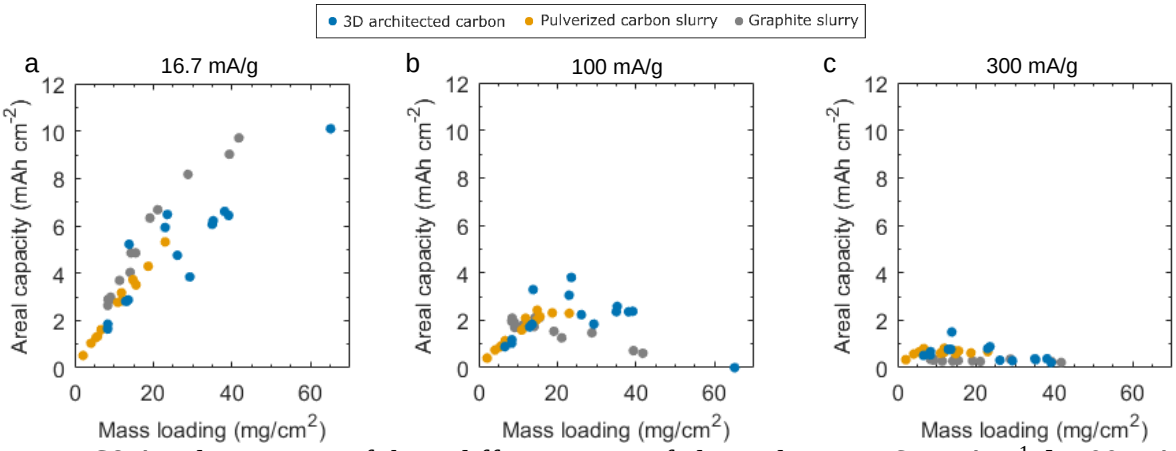

Figure S8 Areal capacities of three different types of electrodes at **a** 16.7 mA g^{-1}, **b** 100 mA g^{-1}, and **c** 300 mA g^{-1}

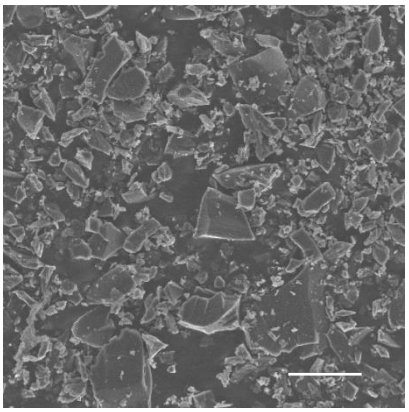

Figure S9 SEM image of pyrolytic carbon particles pulverized from 3D architected carbon. The scale bar is 10 μm.

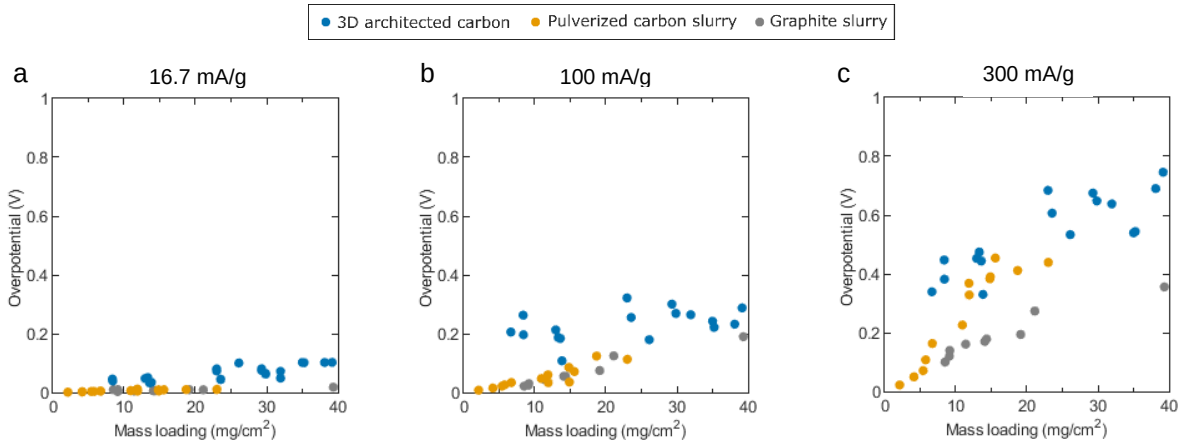

Figure S10 Overpotential vs. mass loading for three different types of electrodes at **a** 16.7 mA g^{-1}, **b** 100 mA g^{-1}, and **c** 300 mA g^{-1}.

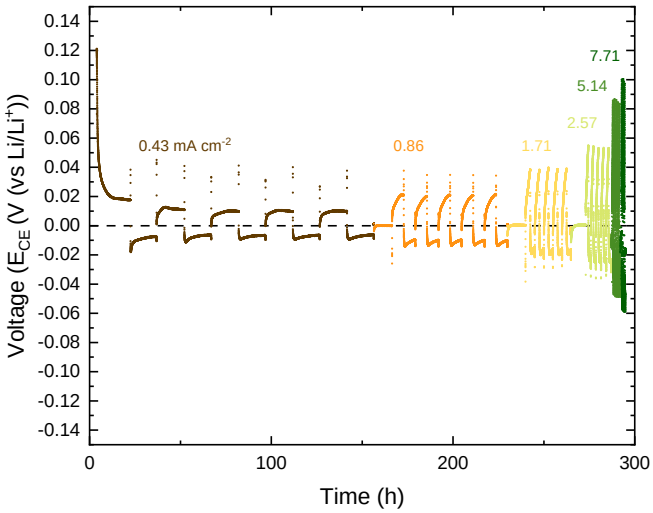

Figure S11 Voltage changes of a lithium counter electrode against a lithium reference electrode in the three-electrode configuration cell with 3D architected carbon working electrode, cycled at step currents shown in Figure S5.

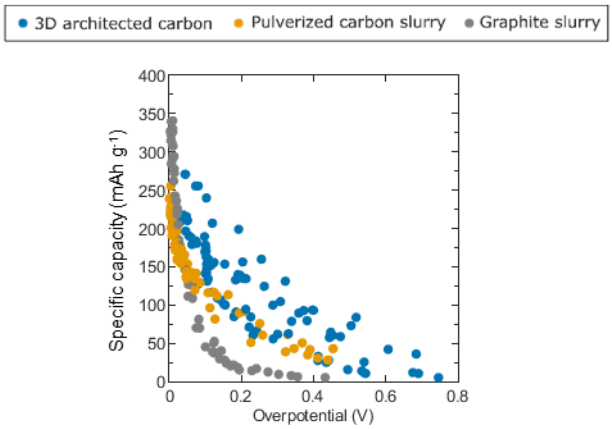

Figure S12 Specific capacities of three types of electrodes with overpotential.

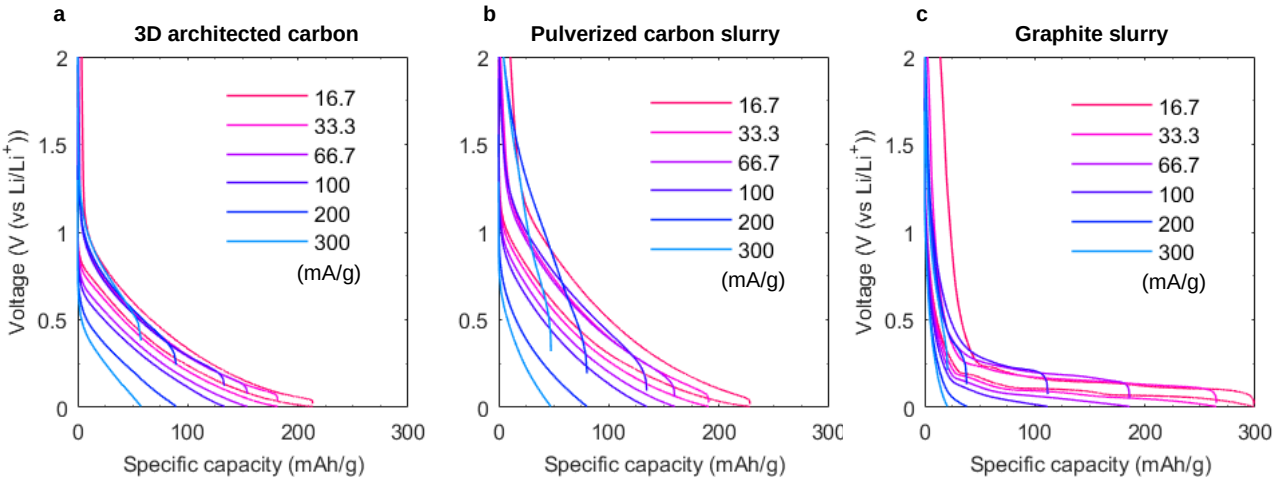

Figure S13 Discharge-charge curves of **a** 3D architected carbon, **b** pulverized carbon slurry and **c** graphite slurry that have around 14 mg cm^{-2} slurry at the 2nd cycle in different current densities. The mass loadings were 13.6 mg cm^{-2} for 3D architected carbon, 15.6 mg cm^{-2} for pulverized carbon slurry, and 14.1 mg cm^{-2} for graphite slurry.

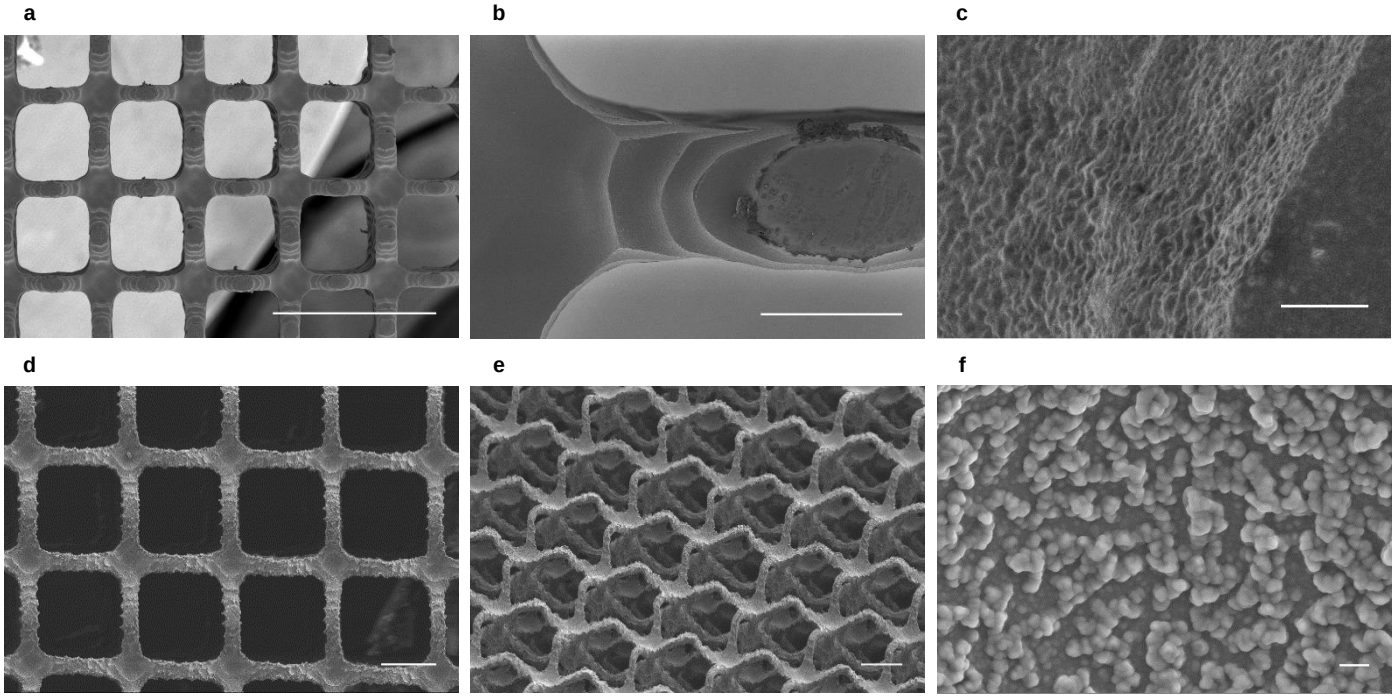

Figure S14 SEM images of **a**, **b**, **c** the 3D polymer after O_2 plasma etching at different magnifications; **d**, **e**, **f** 3D carbon fabricated by pyrolysis of the etched 3D polymer at different magnifications. The scale bars are 1 μm in **a**, 100 μm in **b**, 1 μm in **c**, 100 μm in **d** and **e**, and 1 μm in **f**.

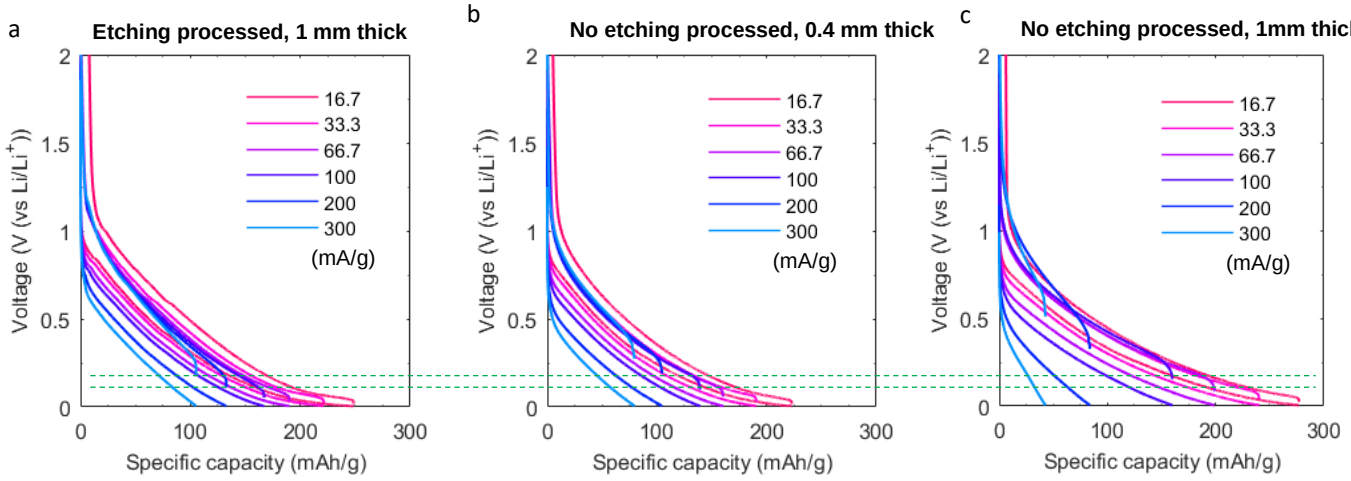

Figure S15 Discharge-charge curves of 3D architected carbon **a** with and **b**, **c** without O2 plasma etching process. The mass loadings of **a** and **b** are similar: 8.25 mg cm^{-2} for **a** and 8.42 mg cm^{-2} for **b**; meanwhile **a** and **c** have similar thickness: 0.996 mm for **a** and 0.973 mm for **c**. Green dot lines show the voltage at the first data acquisition in charge curves at 200 mA g^{-1} (0.1213 V) and 300 mA g^{-1} (0.184 V) for the 3D architected carbon with the etching process.

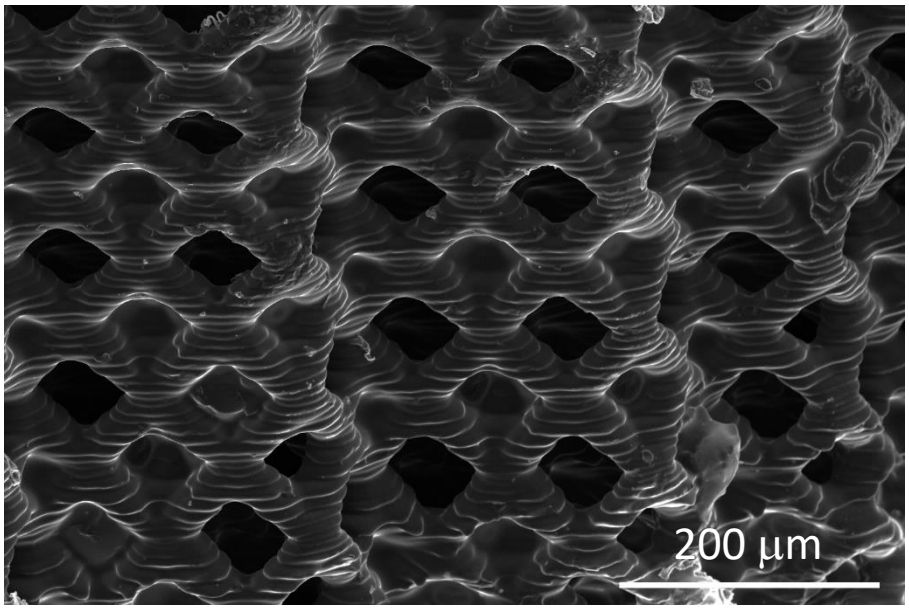

Figure S16 3D architected carbon with 125 μm-wide unit cells.

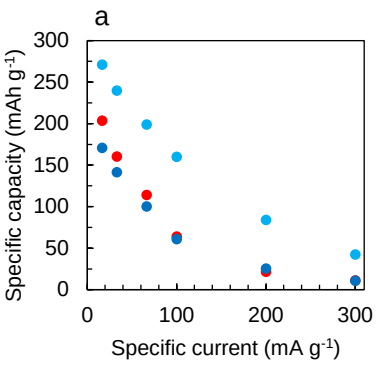

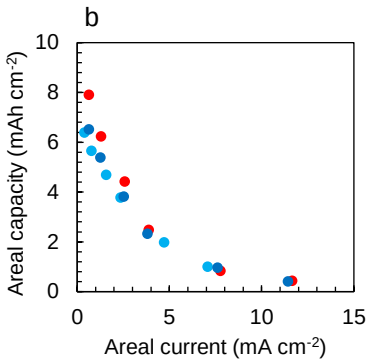

c

Marker	Thickness	Relative density	Mass loading
●	1 mm	35%	38.9 mg cm^{-2}
●	1 mm	10%	24.6 mg cm^{-2}
●	1.4 mm	10%	38.1 mg cm^{-2}

Figure S17 **a** Specific capacity vs specific current, **b** areal capacity vs areal current of architected carbon electrodes, and **c** geometry of the tested carbon electrodes.

Estimation of diffusion length and time

The porosity, ε for 3D architected carbon was set to be the porosity of the designed 3D model in CAD: 10%. The porosities, ε for slurry were calculated by

$$\varepsilon = \frac{mass\ loading}{electrode\ thickness * \rho_b} \quad \text{(S1)}$$

, where ρ_b is a density of bulk materials. The mass loadings and electrode thickness were measured. 2.09 g cm^{-3} is used for the bulk density of graphite and 1.8 g cm^{-3} for pulverized pyrolytic carbon. The bulk density of the pyrolytic carbon was obtained by making a circular plate made of pyrolytic carbon and measuring dimensions and weight. The intrinsic diffusion coefficient used for calculations in Equation (3) are 1.4×10^{-10} $cm^2\ s^{-1}$ for the electrode[1] and 3.2×10^{-6} $cm^2\ s^{-1}$ for the electrolyte[2].

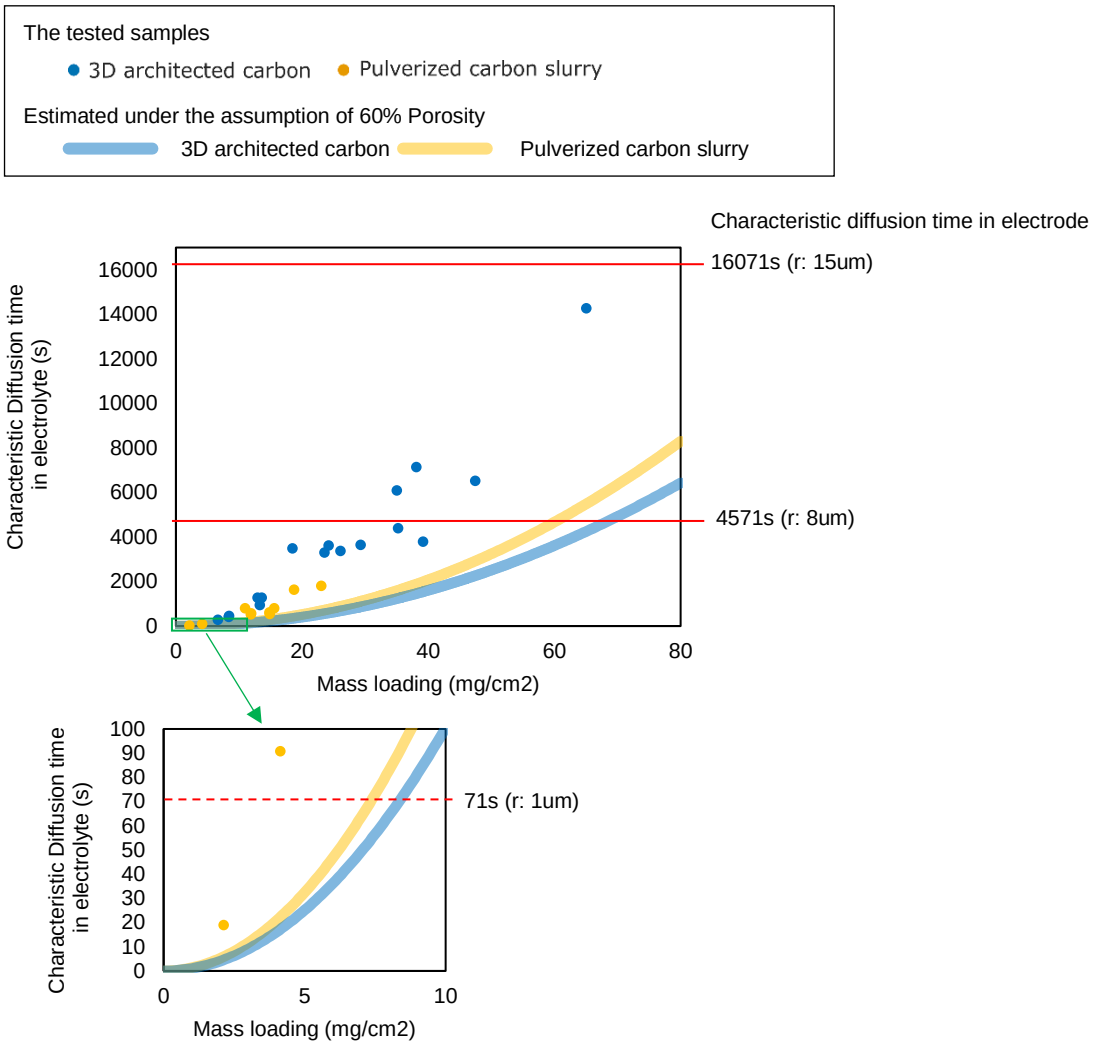

Figure S18 Estimated characteristic diffusion time of Li ion in the electrolyte from tested samples (dots) and electrodes (red lines). Blue and yellow lines show calculated characteristic diffusion time in the electrolyte for 3D architected carbon and pulverized carbon slurry with the assumption of 60% in porosity.

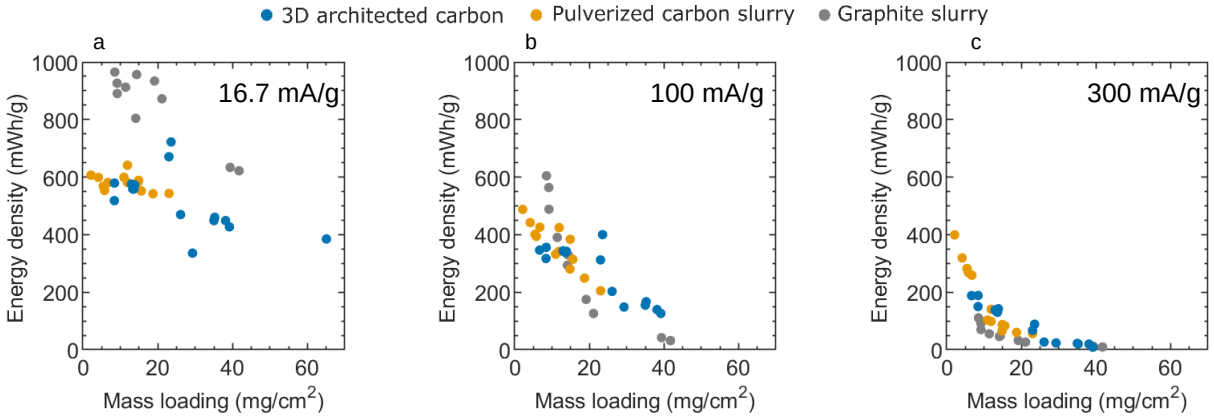

Figure S19 Energy density vs theoretical SHE cathode and mass loading relationship at **a** 16.7 mAg^{-1}, **b** 100 mAg^{-1} and **c** 300 mAg^{-1}

Detail descriptions for Table 1

The detail explanations and the reasons of categories in the electrode engineering factors for each method of structural engineering are described here.

Conventional slurry:
The slurry electrode is the most conventional and commercially employed method. Its components are usually binders and conductive additives in addition to active materials which are randomly stacked. The solid-diffusion length in an electrode corresponds to particle size and can be controlled independently by adjusting it. Tortuosity depends on the calendaring load and resultant porosity because of its randomly stacked geometry. Since the overall structure of stacked particles relies on substantially a calendaring load and resultant structure is random and not designed, the structural integrity is not evaluated.

Slurry with anisotropic pores:
Anisotropic pore structures in slurry electrodes can be created by aligning active materials particles with external fields[3,4] or ice-templating methods [5,6] in the slurry making process. Laser ablating (cutting grooves) into the calendared slurry electrode is also included in this method. These methods can improve tortuosity compared with conventional slurry electrode structures at the same porosity. J. Billaud et al. used a magnetic field to align iron oxide nanoparticles-loaded graphite flakes along the though-thickness direction [3]. Park et al. demonstrated in 2019 that laser structured electrodes enhanced the rate capability of the electrode and specific energy while improving or retaining the power density, due to increased diffusion homogeneity and electrolyte wettability[7].
In this method, tortuosity is not coupled with a fraction of active materials, indicating the independent control capability of the fraction of the active material. However, since tortuosity can be controlled only into a specific range, it is evaluated as a "restricted factor". J. Billaud et al. reported the aligned structure was reorganized by calendaring load [3]; thus the structural integrity is evaluated as "moderate".

Slurry filled in 3D conductive framework:
The 3D conductive framework or 3D current collector is used to support slurry electrodes. It can increase a total electrode thickness and areal mass loading with having a short distance of electron transport between the current collector and active material in contrast to conventional slurry electrodes cast on metallic sheets. This method still requires slurry electrodes composed of randomly packed active particles, binder and conductive additives; the controllable factors are considered in the same way as the conventional slurry electrode. The porous structure of slurry in the 3D current collector is random and not designed like conventional slurry. Therefore, structural integrity is not evaluated.

Planar thin film:
In planer thin film, solid-diffusion length in the electrode can be controlled by simply adjusting the thickness of the film of the active materials. Since there is almost no pores or spaces where electrolyte can be filled in, factors about tortuosity are not evaluated in this method. The structure is a solid film grown on a substrate, which is not designed a complex 3D structure. Therefore, the structural integrity is not evaluated.

Thick monolith:

Thick monolith has been developed recently by W. Lai et al. using lithium cobalt oxide[8]. Since this method relies on necking formation between the polydispersed active material particles via sintering, which changes solid-diffusion length, tortuosity and porosity simultaneously, all electrode engineering factors are dependent relationship. The monolith structure had a high relative density and well-necked structure. Therefore, based on other studies of sintered ceramics [9], we assumed that this structure has good structural integrity even though mechanical properties have not been evaluated for the thick porous monolith made of battery materials.
Tortuosity value is taken from the report about calendared slurry electrodes[10] with a similar fraction of active materials to that of the thick monolith electrode demonstrated by W. Lai et al. [8].

Film on 3D conductive framework:
Another way to use the 3D current collector is by coating active materials on it. The morphology of the 3D current collector ranges from stochastic to periodic structure. H. Zhang et al. coated a thin film of active material on the 3D current collector having inverse opal structure, which enabled the very short diffusion path of ions in the electrode and good electron transport due to the 3D current collector[11]. In a similar manner to planer thin film, the solid-diffusion length in electrode can be controlled independently by adjusting the film thickness, and a fraction of active materials can be controlled by changing the 3D current collector structure such as unit structure size for a periodic structure. H. Zhang et al. showed no structural change of NiOOH on nickel even after 100 cycles at 6C rate; thus, structural integrity is evaluated as "good"[11].
Reference of reported values: solid-diffusion length in electrode and fraction of active materials are from [12,13]. Tortuosity is evaluated as nearly one from the report about tortuosity of periodic inverse opal structure[14]

3D monolith by sacrificial template:
3D porous monolith structures using sacrificial templates have been developed in various template methods, including but not limited to, the usage of monodisperse particles (i.e. inverse opal)[15], bio-template [16], bicontinuous nanoporous alloy[17] and salt-template [18]. Inverse opal structure has the determined tortuosity and active materials fraction (< 26 %), but can control solid-diffusion length by adjusting the wall thickness. Bio-template methods can hardly control all factors because the structure relies on the individuals which could be different. Solid-diffusion length and fraction of active materials are controllable using the method combining bicontinuous nanoporous alloy and selective etching[17]. The usage of the salt particles as a space holder can only control pore size distribution and porosity, but not tortuosity or solid-diffusion length. Applying an external field to align the space holders can allow for low tortuosity (~1) for macro-pores[19]. However, the fabricated monolith had nano/micro-porous which may have high and uncontrollable tortuosity for ion-transport in the filled-in electrolyte. Since there are different methods to fabricate 3D monolith by sacrificial templates with different control capabilities in electrode engineering factors, we adopt the best categories: "independent factor" in solid-diffusion length in electrode from inverse opal structure, "restricted factor" in tortuosity from inverse opal structure and "independent factor" in the fraction of active materials from the usage of space holders. Structural integrity is evaluated as "excellent" from the results of excellent mechanical properties of inverse opal structure[20,21].

Extrusion-based 3D printing:

Three electrode engineering factors in extrusion-based 3D printing were categorized into the correlated factor regardless its macro/micro-control of depositing electrodes because precise control of its nano/micro porous structure of active materials in a wide range has not been demonstrated. The active materials particles' size and fraction are limited to obtain suitable rheological properties to be extruded in a precise manner. The 3D architected silver electrode with a thickness of 400um showed cracks after cycling for 40 times due to volume expansion by 20%, although a 200um thick electrode retained the overall structure. Therefore, we evaluated the structural integrity as "moderate".
Reference of reported values are from [4,22–27] There has not been reported tortuosity values for battery electrodes fabricated by extrusion-based 3D printing.

Lithography-based:
The lithography-based method has been actively investigated toward 3D interdigitated structure. Although reported battery electrodes fabricated by lithography-based techniques showed only 2.5D structure (the structure is only above its substrate geometry), all electrode engineering factors are controllable. This technique is often combined with other methods such as thin-film coating[28] and slurry inclusion[29]. Since each beam arrays are not connected, and mechanical load must be supported by individual beams, especially for share stress, we evaluated its structural integrity as moderate. Full cells using silicon and lithium cobalt oxide showed cracks after cycling due to a significant expansion of silicon upon lithiation[29].

Table 1 with reference numbers

	Solid-diffusion length in electrode (μm)		Tortuosity of diffusion path in electrolyte		Fraction of active materials (v/v)		Structural integrity
Method	min	max	min	max	min	max	
Conventional slurry	0.03[30]	25[31]	1[32]	12[32]	0.3[33]	0.75[33]	-
Slurry with anisotropic pores	0.05[5]	10 [4]	1.3 [5]	6.5[34]	0.24[4]	0.59[35]	Moderate[3]
Slurry filled in 3D conductive framework	0.05[36]	10[37]	1 [38]		0.20[36]	0.35[39]	-
Planar thin film	0.1[40]	15[41]	-	-	-	~1	-
Thick monolith	0.05[42]	2[43]	2[10]	3[10]	0.4[42]	0.87[44]	Good[9]
Film on 3D conductive framework	0.02[12]	0.2[13]	1[14]		0.14[12]	0.69[15]	Good[11]
3D monolith by sacrificial template	0.005[15]	10[18]	1[16]	3.3[18]	0.26[15]	0.68	Excellent[20]
Extrusion-based 3D print	0.1[22]	25[24]			0.06[45]	0.43[4]	Moderate[25]
Lithography-based	0.07[28]	50[46]	1[47]	3[28]	0.08[28]	0.2[29]	Moderate
DLP 3D printing-based (this work)	8	30	1		0.12	0.35	Excellent

Materials:
Conventional slurry: versatile
Particle alignment: LMO[4], LFP[5], Graphite[3], LCO[48], NMC[54]
Slurry filled in 3D current collector: versatile
Planar thin film: versatile
Thick monolith: LTO[49], LCO[44], LFP[42]
Film on 3D current collector: versatile
3D monolith by sacrificial template: versatile
Extrusion-based 3D print: C[50], LMFP[51], LTO[22], LFP[22], LMO[4], Ag[25], S[27]
Lithography-based: C[46], Si[29], Sn[28], LMO[28], LTO[52], LFP[52], LCO[29]

Analytical calculations of required diffusion length in the electrode to shift the rate-limiting process

We analytically calculated the required diffusion length in the electrode to shift the rate-limiting process between diffusion in the electrode vs electrolyte. Electrode thickness, x_{th} can be related to the volume fraction of active material, RD, material density, ρ and mass loading, ML:

$$x_{th} = \frac{ML}{RD \times \rho} \quad \text{(S2)}$$

Rate-limiting process may be shifted when characteristic diffusion time in electrode and electrolyte are equivalent:

$$\frac{x_{rad}^2}{D_0^s} = \frac{x_{th}^2}{D_{eff}^l} \quad \text{(S3)}$$

where $x_{rad}$is the beam radius of architected carbon, D_0^s is the intrinsic diffusivity in carbon electrode, D_{eff}^l is the effective diffusivity in the electrolyte filled in the porous electrode. Using Eqs S2, S3 and Equation (2) in the main manuscript, we can obtain the required beam radius, x_{rad} to shift rate-limiting process between transport within electrolyte vs. electrode, expressed by mass loading, ML and active material fraction, RD

$$x_{rad} = \sqrt{\frac{D_0^s}{D_0^l} \times \frac{1}{1-RD} \times \left(\frac{ML}{RD \times \rho}\right)^2} \quad \text{(S4)}$$

where D_0^s is the intrinsic diffusivity in the electrolyte. Here we assume that tortuosity of architected carbon is unity due to its straight pore structure.

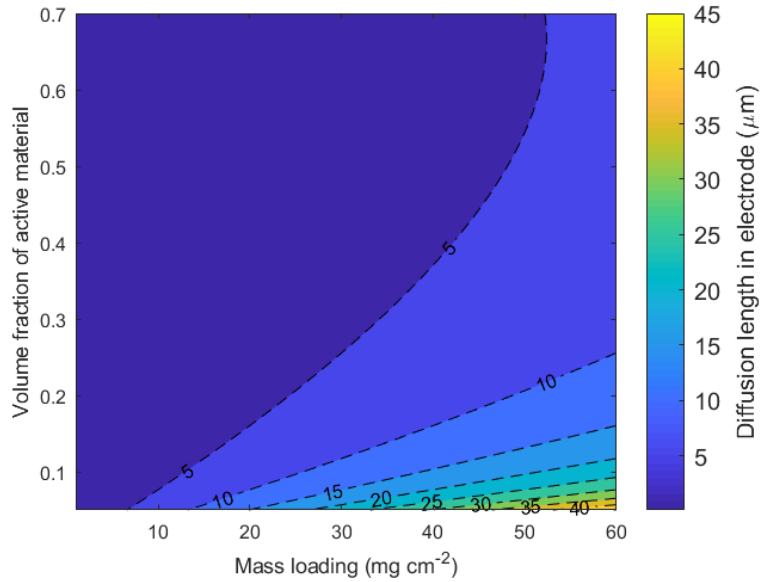

Figure S20 Required diffusion length in the electrode to shift the rate-limiting process between transport in the electrode vs electrolyte as a function of a volume fraction of active materials and mass loading

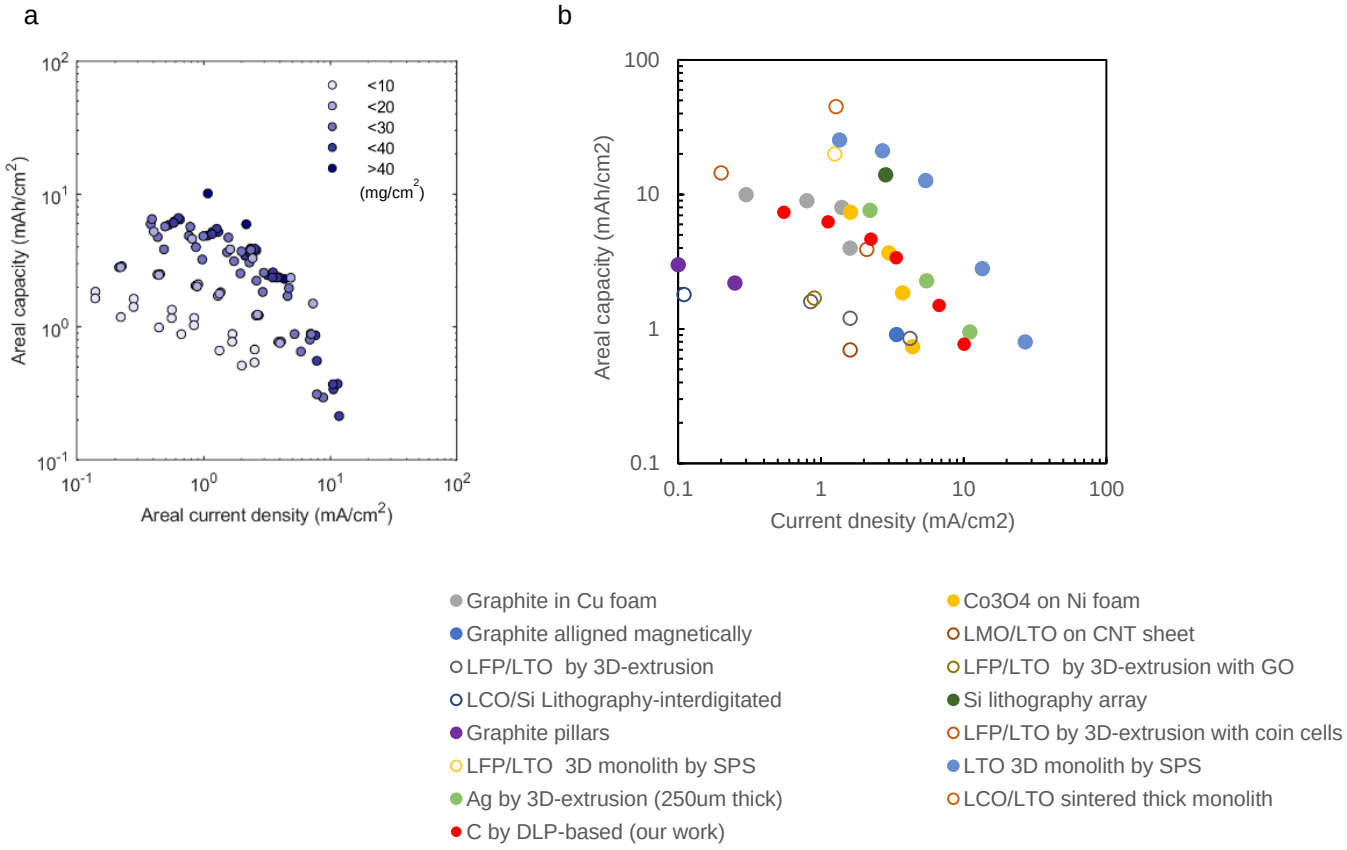

Figure S21 Ragone plots of **a** the 3D architected carbon electrode with different mass loadings, and **b** anode half cells (closed circle) and full cells (open circle) assembled with structurally engineered electrodes

References: Graphite in Cu foam[37], Co3O4 anode on Ni foam[55], Graphite aligned magnetically[3], LMO/LTO on CNT sheet[56], LFP/LTO by 3D-extrusion[22], LFP/LTO by 3D-extrusion with GO[23], LCO/Si lithography-interdigitated[29], Si lithography array[29], Graphite pillars[46], LFP/LTO by 3D-extrusion with coin cells[26], LFP/LTO 3D monolith by SPS[57], LTO 3D monolith by SPS[57], Ag by 3D-extrusion (250um thick)[25], LCO/LTO sintered thick monolith[58]

Analytical calculations of volumetric capacity of a planar cell and 3D interdigitated cell

We analytically calculated attainable volumetric capacity of a conventional planar full cell and 3D interdigitated full cell composed of pyrolytic carbon (250 mAh g^{-1}, 1.8 g cm^{-3}) and lithium iron phosphate (170 mAh g^{-1}, 3.5 g cm^{-3}). In a planar cell, we determined the cathode electrode thickness, L_c by matching capacities between the anode and cathode:

$$L_c = \frac{q_a \rho_a L_a \theta_a}{q_c \rho_c \theta_c} \qquad \text{R(5)}$$

where L is the electrode thickness, ρ is the material density, θ is the volume fraction of active materials, and subscripts a and c denote the anode electrode and cathode electrode, respectively. We assume that 70 vol.% of active materials in the cathode electrode. Volumetric capacity, Q_v is calculated by dividing areal capacity by cell thickness composed of anode and cathode electrodes and simplified:

$$Q_v^{planar} = \frac{q_a \rho_a \theta_a \times q_c \rho_c \theta_c}{q_a \rho_a \theta_a + q_c \rho_c \theta_c} \qquad \text{R(7)}$$

We do not consider a separator and current collector to calculate volumetric capacity.
For an interdigitated electrode cell, since the anode thickness and cathode thickness are equivalent, the volumetric capacity of an interdigitated cell, Q_v^{id} can be expressed by

$$Q_v^{id} = q_a \rho_a \theta_a = q_c \rho_c \theta_c \qquad \text{R(8)}$$

with feasible volume fractions of active materials (i.e. $\theta_a + \theta_c < 1$) in the capacity-matched anode and cathode.

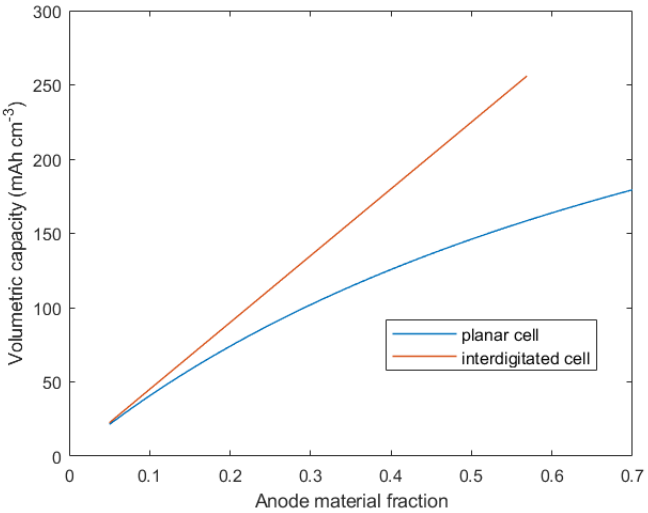

Figure S22 Volumetric capacity change upon anode materials fraction for planar cell and interdigitated cell composed of pyrolytic carbon anode and lithium iron phosphate cathode materials

References

[1] H. jun GUO, X. hai LI, X. ming ZHANG, H. qiang WANG, Z. xing WANG, W. jie PENG, *New Carbon Mater.* **2007**, *22*, 7.

[2] L. O. Valøen, J. N. Reimers, *J. Electrochem. Soc.* **2005**, *152*, A882.

[3] J. Billaud, F. Bouville, T. Magrini, C. Villevieille, A. R. Studart, *Nat. Energy* **2016**, *1*, 1.

[4] J. Li, X. Liang, F. Liou, J. Park, *Sci. Rep.* **2018**, *8*, 1.

[5] C. Huang, M. Dontigny, K. Zaghib, P. S. Grant, *J. Mater. Chem. A* **2019**, *7*, 21421.

[6] C. Huang, P. S. Grant, *J. Mater. Chem. A* **2018**, *6*, 14689.

[7] J. Park, S. Hyeon, S. Jeong, H. J. Kim, *J. Ind. Eng. Chem.* **2019**, *70*, 178.

[8] W. Lai, C. K. Erdonmez, T. F. Marinis, C. K. Bjune, N. J. Dudney, F. Xu, R. Wartena, Y. M. Chiang, *Adv. Mater.* **2010**, *22*, 139.

[9] M. MUNRO, *J. Am. Ceram. Soc.* **2005**, *80*, 1919.

[10] C. Lim, B. Yan, H. Kang, Z. Song, W. C. Lee, V. De Andrade, F. De Carlo, L. Yin, Y. Kim, L. Zhu, *J. Power Sources* **2016**, *328*, 46.

[11] H. Zhang, X. Yu, P. V Braun, *Nat. Nanotechnol.* **2011**, *6*, 277.

[12] J. H. Pikul, H. Gang Zhang, J. Cho, P. V. Braun, W. P. King, *Nat. Commun.* **2013**, *4*, 1732.

[13] H. Zhang, X. Yu, P. V Braun, *Nat. Nanotechnol.* **2011**, *6*, 277.

[14] S. Suter, S. Haussener, *Energy Environ. Sci.* **2019**, *12*, 1668.

[15] K. T. Lee, J. C. Lytle, N. S. Ergang, S. M. Oh, A. Stein, *Adv. Funct. Mater.* **2005**, *15*, 547.

[16] L. L. Lu, Y. Y. Lu, Z. J. Xiao, T. W. Zhang, F. Zhou, T. Ma, Y. Ni, H. Bin Yao, S. H. Yu, Y. Cui, *Adv. Mater.* **2018**, *30*, 1.

[17] C. Wang, Q. Chen, *Chem. Mater.* **2018**, *30*, 3894.

[18] R. Elango, A. Demortière, V. De Andrade, M. Morcrette, V. Seznec, *Adv. Energy Mater.* **2018**, *1703031*, 1.

[19] J. S. Sander, R. M. Erb, L. Li, A. Gurijala, Y. M. Chiang, *Nat. Energy* **2016**, *1*, 1.

[20] J.-H. Lee, L. Wang, M. C. Boyce, E. L. Thomas, *Nano Lett.* **2012**, *12*, 4392.

[21] J. H. Pikul, S. Özerinç, B. Liu, R. Zhang, P. V. Braun, V. S. Deshpande, W. P. King, *Sci. Rep.* **2019**, *9*, 1.

[22] K. Sun, T. S. Wei, B. Y. Ahn, J. Y. Seo, S. J. Dillon, J. A. Lewis, *Adv. Mater.* **2013**, *25*, 4539.

[23] K. Fu, Y. Wang, C. Yan, Y. Yao, Y. Chen, J. Dai, S. Lacey, Y. Wang, J. Wan, T. Li, Z. Wang, Y. Xu, L. Hu, *Adv. Mater.* **2016**, *28*, 2587.

[24] J. Li, M. C. Leu, R. Panat, J. Park, *Mater. Des.* **2017**, *119*, 417.

[25] M. S. Saleh, J. Li, J. Park, R. Panat, *Addit. Manuf.* **2018**, *23*, 70.

[26] T.-S. Wei, B. Y. Ahn, J. Grotto, J. A. Lewis, *Adv. Mater.* **2018**, *1703027*, 1703027.

[27] K. Shen, H. Mei, B. Li, J. Ding, S. Yang, *Adv. Energy Mater.* **2018**, *8*, 1.

[28] H. Ning, J. H. Pikul, R. Zhang, X. Li, S. Xu, J. Wang, J. A. Rogers, W. P. King, P. V. Braun, *Proc. Natl. Acad. Sci. U. S. A.* **2015**, *112*, 6573.

[29] J. I. Hur, L. C. Smith, B. Dunn, *Joule* **2018**, 1.

[30] B. Kang, G. Ceder, *Nature* **2009**, *458*, 190.

[31] B. Bitsch, J. Dittmann, M. Schmitt, P. Scharfer, W. Schabel, N. Willenbacher, *J. Power Sources* **2014**, *265*, 81.

[32] M. Ebner, D. W. Chung, R. E. García, V. Wood, *Adv. Energy Mater.* **2014**, *4*, 1.

[33] T. Marks, S. Trussler, A. J. Smith, D. Xiong, J. R. Dahn, *J. Electrochem. Soc.* **2011**, *158*, A51.

[34] L. Kraft, J. B. Habedank, A. Frank, A. Rheinfeld, A. Jossen, *J. Electrochem. Soc.* **2020**, *167*, 013506.

[35] K. H. Chen, M. J. Namkoong, V. Goel, C. Yang, S. Kazemiabnavi, S. M. Mortuza, E.

Kazyak, J. Mazumder, K. Thornton, J. Sakamoto, N. P. Dasgupta, *J. Power Sources* **2020**, *471*, 228475.
[36] H. Ji, L. Zhang, M. T. Pettes, H. Li, S. Chen, L. Shi, R. Piner, R. S. Ruoff, *Nano Lett.* **2012**, *12*, 2446.
[37] J. S. Wang, P. Liu, E. Sherman, M. Verbrugge, H. Tataria, *J. Power Sources* **2011**, *196*, 8714.
[38] B. Shi, Y. Shang, Y. Pei, S. Pei, L. Wang, D. Heider, Y. Y. Zhao, C. Zheng, B. Yang, S. Yarlagadda, T. Chou, K. K. Fu, *Nano Lett.* **2020**, *20*, 5504.
[39] X. Guan, Z. Zhang, S. Zhang, Y. Wang, H. Yang, J. Wang, M. Li, H. Lu, Y. Li, Q. Huang, X. Zheng, Z. Qiao, Z. Yu, J. Kang, *Electrochim. Acta* **2019**, *312*, 424.
[40] Y. N. Zhou, M. Z. Xue, Z. W. Fu, *J. Power Sources* **2013**, *234*, 310.
[41] J. B. Bates, N. J. Dudney, B. Neudecker, A. Ueda, C. D. Evans, *Solid State Ionics* **2000**, *135*, 33.
[42] X. Qin, X. Wang, J. Xie, L. Wen, *J. Mater. Chem.* **2011**, *21*, 12444.
[43] C. J. Bae, C. K. Erdonmez, J. W. Halloran, Y. M. Chiang, *Adv. Mater.* **2013**, *25*, 1254.
[44] W. Lai, C. K. Erdonmez, T. F. Marinis, C. K. Bjune, N. J. Dudney, F. Xu, R. Wartena, Y. M. Chiang, *Adv. Mater.* **2010**, *22*, 139.
[45] C. Sun, S. Liu, X. Shi, C. Lai, J. Liang, Y. Chen, *Chem. Eng. J.* **2020**, *381*, 122641.
[46] N. Cirigliano, G. Sun, D. Membreno, P. Malati, C. J. Kim, B. Dunn, *Energy Technol.* **2014**, *2*, 362.
[47] C. Wang, L. Taherabadi, G. Jia, M. Madou, Y. Yeh, B. Dunn, *Electrochem. Solid-State Lett.* **2004**, *7*, A435.
[48] L. Li, R. M. Erb, J. Wang, J. Wang, Y. M. Chiang, *Adv. Energy Mater.* **2019**, *9*, DOI 10.1002/aenm.201802472.
[49] J. P. Robinson, J. J. Ruppert, H. Dong, G. M. Koenig, *J. Appl. Electrochem.* **2018**, *48*, 1297.
[50] A. Maurel, M. Courty, B. Fleutot, H. Tortajada, K. Prashantha, M. Armand, S. Grugeon, S. Panier, L. Dupont, *Chem. Mater.* **2018**, *30*, 7484.
[51] J. Hu, Y. Jiang, S. Cui, Y. Duan, T. Liu, H. Guo, L. Lin, Y. Lin, J. Zheng, K. Amine, F. Pan, *Adv. Energy Mater.* **2016**, *6*, DOI 10.1002/aenm.201600856.
[52] E. Cohen, S. Menkin, M. Lifshits, Y. Kamir, A. Gladkich, G. Kosa, D. Golodnitsky, *Electrochim. Acta* **2018**, *265*, 690.
[53] K. H. Chen, M. J. Namkoong, V. Goel, C. Yang, S. Kazemiabnavi, S. M. Mortuza, E. Kazyak, J. Mazumder, K. Thornton, J. Sakamoto, N. P. Dasgupta, *J. Power Sources* **2020**, *471*, 228475.
[54] M. Bolsinger, M. Weller, S. Ruck, P. Kaya, H. Riegel, V. Knoblauch, *Electrochim. Acta* **2020**, *330*, DOI 10.1016/j.electacta.2019.135163.
[55] X. Wang, Y. Fan, R. Agung Susantyoko, Q. Xiao, L. Sun, D. He, Q. Zhang, *Nano Energy* **2014**, *5*, 91.
[56] W. Weng, Q. Sun, Y. Zhang, S. He, Q. Wu, J. Deng, X. Fang, G. Guan, J. Ren, H. Peng, *Adv. Mater.* **2015**, *27*, 1363.
[57] R. Elango, A. Demortière, V. De Andrade, M. Morcrette, V. Seznec, *Adv. Energy Mater.* **2018**, *1703031*, 1.
[58] J. P. Robinson, J. J. Ruppert, H. Dong, G. M. Koenig, *J. Appl. Electrochem.* **2018**, *48*, 1297.